Topographic and Boundary Influences on the 22 May 2014 Duanesburg, New York, Tornadic Supercell

BRIAN TANG, MATTHEW VAUGHAN, ROSS LAZEAR, KRISTEN CORBOSIERO, AND LANCE BOSART

Department of Atmospheric and Environmental Sciences, University at Albany, State University of New York, Albany, New York

THOMAS WASULA, IAN LEE, AND KEVIN LIPTON

NOAA/National Weather Service, Albany, New York

ABSTRACT

The 22 May 2014 Duanesburg, New York, supercell produced an enhanced Fujita scale category 3 (EF3) tornado and 10-cm-diameter hail. The synoptic setup for the event was ambiguous compared to other documented cases of Northeast tornadoes. Mesoscale inhomogeneities due to terrain and baroclinic boundaries played a key role in the evolution and severity of the storm. The storm initiated at the intersection of an outflow boundary and a north–south-oriented baroclinic boundary. The mesocyclone was able to sustain itself as a result of sufficiently large amounts of low-level streamwise vorticity near the boundary despite subcritical values of 0–6-km vertical wind shear. Differential heating across the north–south-oriented boundary strengthened the pressure gradient across it. Strengthening ageostrophic flow across the boundary induced greater upslope flow along the southeastern slope of the Adirondack Mountains and induced terrain channeling up the Mohawk River valley. The channeling led to a maximum in moisture flux convergence and instability in the Mohawk valley. As the supercell moved into the Mohawk valley, radar and lightning data indicated a rapid intensification of the storm. Cold temperatures aloft due to the presence of an elevated mixed layer (EML) coincided with the surface instability to yield a local environment in the Mohawk valley favorable for extremely large hail. As the storm crossed the boundary, large values of 0–1-km wind shear, streamwise vorticity, and low lifting condensation levels combined to create a local environment favorable for tornadogenesis.

---

1. Introduction

New York has averaged about 10 tornadoes per year over the period from 1985 to 2014 (Carbin 2015). Only eight tornadoes during this same period have been rated category 3 or higher on the Fujita/enhanced Fujita scales (F/EF3; NOAA 2015). One of those tornadoes occurred on 22 May 2014, when an EF3 tornado hit the towns of Duanesburg and Delanson, New York. Additionally, the same supercell produced 10-cm-diameter hail in Amsterdam, New York, tying the New York State record previously set on 27 September 1998 in Niagara Falls (NOAA 2015). Such a high-end event had low predictive

skill, making this particular case interesting and important to understand.

Forecasting severe weather in the Northeast presents unique challenges because of the complex terrain. Figure 1 shows a topographic map annotated with key terrain features important for this study. The Hudson River valley is a prominent north–south-oriented valley. The Mohawk River valley branches off the Hudson valley toward the west in the center of the figure. The Adirondack Mountains lie to the north of the Mohawk valley, and the Catskill Mountains lie to the south of the Mohawk valley.

The interaction of terrain with convection is important for assessing local areas that have a heightened risk for impacts when the synoptic-scale conditions favor severe weather. Maxima in severe weather reports, radar reflectivity, and lightning strike densities have preferential locations in the Northeast depending on the direction of the synoptic-scale flow relative to the underlying terrain (Wasula et al. 2002; Murray and Colle

Corresponding author address: Brian Tang, Dept. of Atmospheric and Environmental Sciences, University at Albany, State University of New York, ES 324, 1400 Washington Ave., Albany, NY 12222.
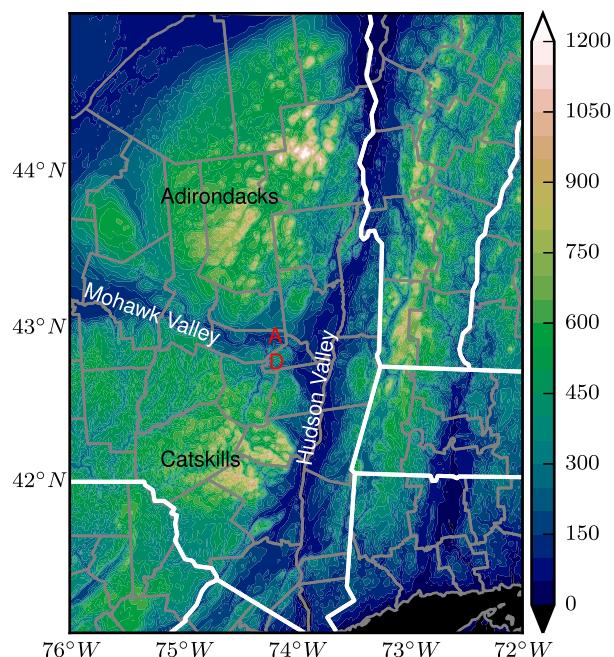E-mail: btang@albany.edu

FIG. 1. Topography of the region of interest. Elevation (m) is shaded. The A is the location of Amsterdam, and the D is the location of Duanesburg.

2011). Supercells, in particular, may strengthen where they intersect areas of enhanced low-level shear or storm-relative helicity caused by channeled flow in valleys (Braun and Monteverdi 1991; LaPenta et al. 2005; Bosart et al. 2006; Geerts et al. 2009; Peyraud 2013). The channeled flow can also advect moist, unstable air into the inflow of a supercell (Riley and Bosart 1987; LaPenta et al. 2005). Furthermore, upslope and downslope flow can modulate the intensity of supercells. Markowski and Dotzek (2011) show that upslope flow reduces convective inhibition and increases relative humidity, leading to a transient increase in updraft speed and relative vorticity in idealized simulations of a supercell. Conversely, weakening occurs in regions of downslope flow. Orographically generated environmental cyclonic vertical vorticity anomalies, such as lee vortices and shear lines, may also increase the low-level vertical vorticity of a supercell (Geerts et al. 2009; Markowski and Dotzek 2011).

Baroclinic boundaries have been hypothesized to affect supercell evolution and tornadogenesis. Such boundaries may arise from synoptic fronts and outflow boundaries from prior convection. Additionally, boundaries may be modified by terrain interactions. Mesoscale maxima in moisture convergence and vertical vorticity along the boundary may then provide a locally favorable environment for supercells to intensify as they cross such boundaries (Maddox et al. 1980). In fact, 70% of tornadoes during the Verification of the Origins of

Rotation in Tornadoes Experiment (VORTEX) occurred as supercells crossed boundaries, particularly on the cool side <30 km from the boundary (Markowski et al. 1998). Buoyancy gradients across the boundary lead to an increase in horizontal vorticity. When the horizontal vorticity is streamwise, having a component in the same direction as the storm-relative inflow, the horizontal vorticity is tilted into the vertical to produce mesocyclone rotation (Rasmussen et al. 2000). Storms that propagate along the boundary form the strongest and most persistent mesocyclones, and a significant source of streamwise vorticity originates from the cool side of the boundary (Atkins et al. 1999).

The Duanesburg supercell interacted with a variety of terrain and baroclinic boundaries, making its evolution complex and difficult to predict. Section 2 gives an overview of the supercell's timeline. In contrast to existing Northeast tornado case studies, such as the 1979 Windsor Locks, Connecticut, tornado (Riley and Bosart 1987); the 1995 Great Barrington, Massachusetts, tornado (Bosart et al. 2006); the 1998 Mechanicville, New York, tornado (LaPenta et al. 2005); and the 2011 Springfield, Massachusetts, tornado (Banacos et al. 2012), the antecedent synoptic-scale setup did not strongly suggest the possibility for this event, let alone its severity. Section 3 details specific ingredients in the synoptic setup that were present and absent.

The absence of regional synoptic-scale favorability for severe weather suggests mesoscale inhomogeneities induced by the terrain and baroclinic boundaries aligned in such a way to favor this event. We will use 3-km High Resolution Rapid Refresh (HRRR) analyses[1] combined with conventional surface observations to diagnose important mesoscale inhomogeneities. Lightning and radar data will be used to link where these mesoscale inhomogeneities may have had an effect on the supercell evolution. Section 4 focuses on the initiation and early phases of the supercell, and section 5 focuses on the large hail and tornadic phases of the supercell. Section 6 follows with conclusions.

2. Storm timeline

Convective initiation occurred shortly after 1515 UTC in the Adirondacks (Fig. 2). From initiation to 1700 UTC, reflectivities and the areal extent of the cell increased while the cell traveled toward the south-southeast over

---

[1] The HRRR model became operational at NOAA/NWS/ NCEP/Environmental Modeling Center (EMC) on 30 September 2014. Analyses are from the preoperational version of the model from the NOAA/Earth System Research Laboratory.
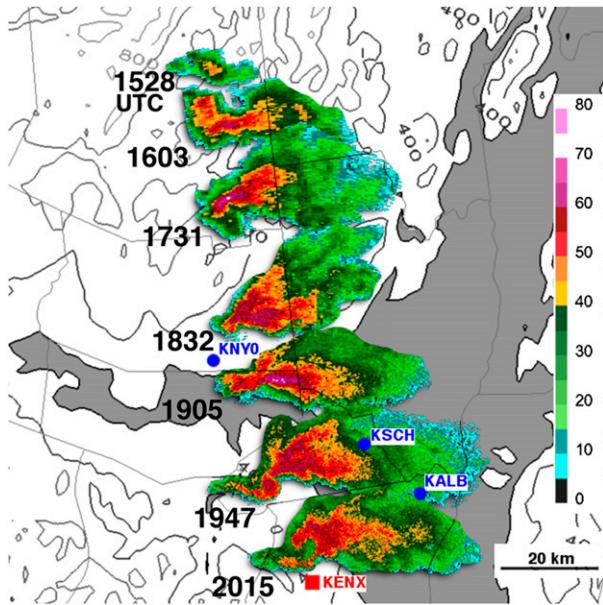
FIG. 2. KENX 0.5°-elevation reflectivity (dBZ) montage of the Duanesburg supercell. Times are given to the left of each snapshot. Elevation is contoured every 200 m, with elevations under 200 m shaded in gray. Locations of key surface observation stations (KNY0, KSCH, and KALB; blue circles) and the KENX radar (red square) are also given.

the southern Adirondacks. The cell acquired broad, weak rotation (Fig. 3) with differential velocities generally between 5 and 15 m s^{-1}. The low-level differential velocity is defined as the difference between the maximum outbound and minimum inbound velocities of the cell in the 0.5°-elevation radial velocity from the Albany, New York, radar (KENX). The midlevel differential velocity is defined as the difference between the maximum outbound

and minimum inbound velocities at a fixed height of 5 km and a maximum horizontal separation of 10 km. Cloud-to-ground (CG) lightning flashes from the National Lightning Detection Network (NLDN; Cummins and Murphy 2009) are binned every 4 min, centered on the time of the 0.5° radar scans.

There was a general intensification trend in both the low-level and midlevel differential velocities through 2000 UTC. The movement of the cell was toward the radar, so the lowest sampled height decreased from 2.2 to 0.7 km above mean sea level over the period. Moreover, the radar data increased in resolution as the storm approached the radar location. Both of these factors may have caused a portion of the intensification trend, but were unlikely to be the sole explanations. Reflectivities, the storm structure, CG lightning activity, and severe weather reports all supported the intensification trend as well.

Between 1700 and 1800 UTC, the cell strengthened as it moved off the higher terrain of the Adirondacks into the northern side of the Mohawk valley. Reflectivities continued to increase, reaching a local maximum of 70 dBZ at 1731 UTC (Fig. 2). Concurrently, there was a sharp increase in low-level differential velocity, peaking at 27 m s^{-1}. The midlevel differential velocity also doubled to 20 m s^{-1} during this hour. Lightning activity increased up to 8 flashes (4 min)$^{-1}$ (Fig. 3).

After 1800 UTC, the low-level and midlevel differential velocities both briefly weakened, but quickly cycled upward in intensity to 30 and 40 m s^{-1} after 1830 UTC, respectively. During the intensification of the mesocyclone, there was a spike in lightning around 1830 UTC. The first severe hail reports occurred around this time and increased considerably after 1900 UTC. The 10-cm
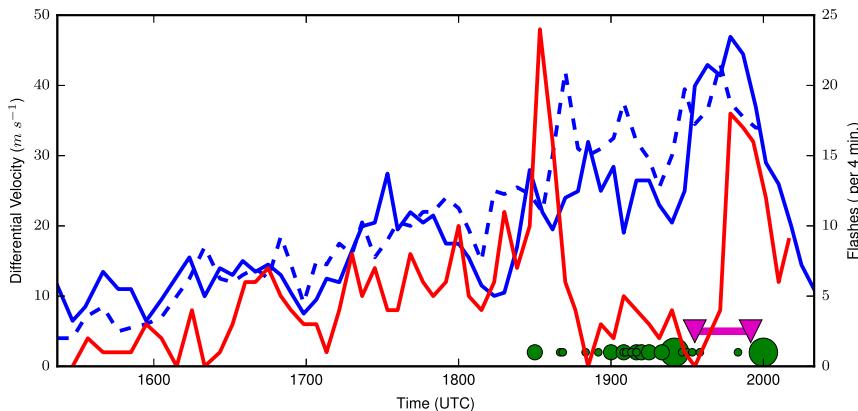

FIG. 3. Time series of the low-level (blue, solid) and midlevel (blue, dashed) mesocyclone differential velocities and NLDN CG lightning flash counts per four minutes (red). See text for definitions. Severe hail reports are denoted by green circles (small circle, 2.5–5 cm; medium circle, 5–7.5 cm; and large circle, ≥7.5 cm), and tornado start and end times are denoted by purple triangles.
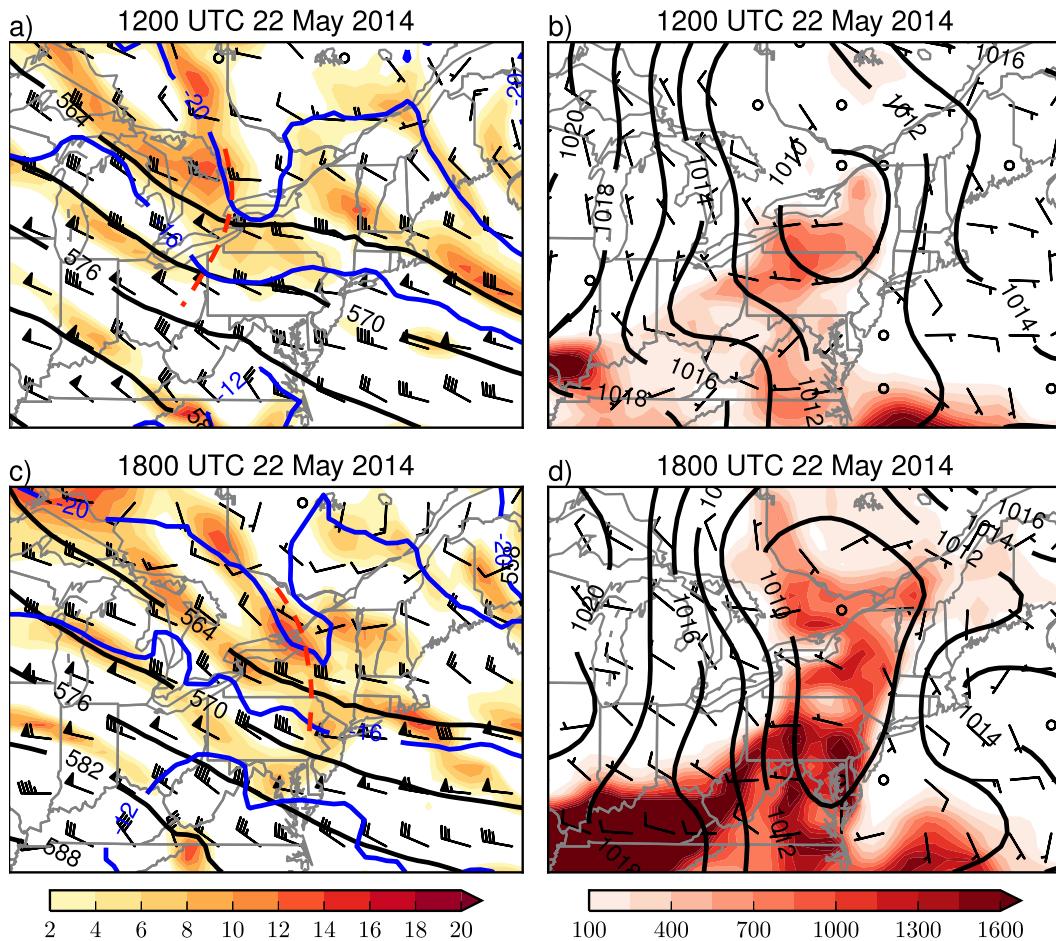
FIG. 4. The 1200 UTC 22 May 2014 GFS analysis of (a) 0–6-km wind shear (barbs; m s^{-1}), geopotential heights (black contours; dm), temperature (blue contours; °C), and relative vorticity (shaded; $\times 10^{-5}$ s^{-1}), and (b) surface wind (barbs; m s^{-1}), mean sea level pressure (contours; hPa), and surface-based CAPE (shaded; J kg^{-1}). (c),(d) As in (a),(b), respectively, but at 1800 UTC 22 May 2014. The short-wave troughs in (a) and (c) are given by the dashed, red line.

hailstone was reported at 1925 UTC. There was little lightning activity during the time interval of the highest density of the hail reports, which will be discussed later.

The tornadic phase of the supercell began at 1928 UTC. The low-level differential velocity increased rapidly to a maximum of 47 m s^{-1}. The tornado formed at 1933 UTC, causing EF3 damage at one location before dissipating at 1955 UTC. After 2000 UTC, the low-level differential velocity and lightning activity quickly diminished as the supercell weakened and moved into the northern Catskills.

3. Antecedent conditions

a. Synoptic setup

While there were some signals for severe weather in the synoptic setup, the factors were generally ambiguous. There was broad 500-hPa northwesterly flow over the Northeast (Fig. 4a) on the backside of a long-wave trough. The flow speed ranged from 5 to 20 m s^{-1} from north to south across New York. As a result, the 0–6-km bulk wind shear was 5–20 m s^{-1} north of the Mohawk valley and 20–25 m s^{-1} south of the Mohawk valley. A weak short-wave trough was embedded within the northwesterly flow over southern Ontario at 1200 UTC. There was also a pocket of cold air at 500 hPa just east of the short-wave trough.

The cold air aloft was observed in the 1200 UTC Buffalo, New York, sounding (Fig. 5a). The 500-hPa temperature at Buffalo at 1200 UTC was −19.1°C, which falls below the 25th percentile for 1200 UTC 22 May (Rogers et al. 2015). The anomalously cold air coincided with the top of an elevated mixed layer (EML). In fact, there were two prominent EMLs separated by a small inversion. The lower EML extended from 860 to 680 hPa with a mean lapse rate of 8.8°C km^{-1}, and the upper EML extended from 620 to 500 hPa with a mean lapse rate of 9.2°C km^{-1}.
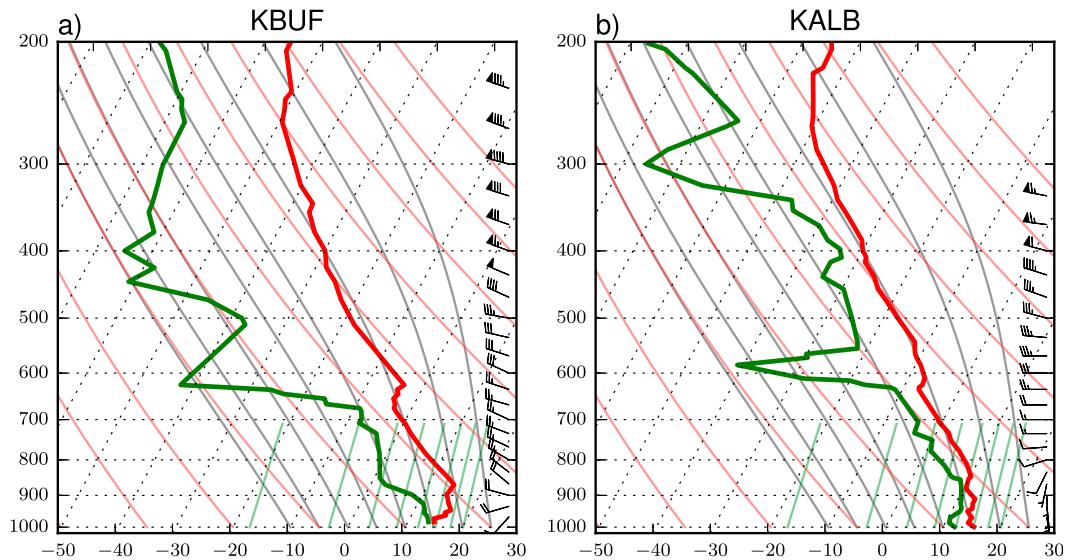
FIG. 5. The 1200 UTC 22 May 2014 skew T–log$p$ soundings from (a) Buffalo and (b) Albany.

EMLs are one potentially important ingredient for severe weather outbreaks, providing a source of potential instability that can be released by forcing for ascent (Farrell and Carlson 1989; Colle et al. 2012). Steep low- to midlevel lapse rates tied to EMLs are conducive for severe hail in the Northeast (Banacos and Ekster 2010; Hurlbut and Cohen 2014). Additionally, Johns and Dorr (1996) find that some significant tornadoes in New England and eastern New York occur in 500-hPa northwesterly flow regimes in the presence of an EML, although such tornado events are rare compared to events in southwesterly and westerly flow regimes. For this event, the EML was the strongest signal for severe weather in the synoptic picture.

At the surface at 1200 UTC, a broad area of low pressure coinciding with an instability ridge (Fig. 4b) protruded into the southwest portions of the Northeast. A cool and stable maritime air mass, characterized by equivalent potential temperatures less than 315 K (not shown), covered most of New England. Between the maritime air mass and a more unstable air mass to the west, there was a north–south-oriented boundary aligned with the Hudson valley. This boundary is hypothesized to be a key feature in the evolution of the supercell.

The 1200 UTC Albany sounding was representative of the cool side of the boundary relative to areas just to the west (Fig. 5b). Below 900 hPa, southerly winds advected cool, moist air up the Hudson valley. The Albany sounding had steep lapse rates of 7.8°C km^{-1} in the 830–630-hPa layer. The low-level advection of the

maritime air mass and capping inversion below the modified EML kept the boundary layer cool and moist. As a result, low-level stratus with cloud bases of 350–450 m above ground level remained at Albany through 2100 UTC.

The short-wave trough moved across New York from 1200 to 1800 UTC (Fig. 4c). Cyclonic vorticity advection ahead of the short-wave trough may have aided in triggering convection over the Adirondacks. The pocket of cold air aloft also shifted eastward, spreading over the area of the supercell. The associated surface trough elongated meridionally and remained centered over New York (Fig. 4d). The surface-based convective available potential energy (CAPE) increased to 500–1200 J kg^{-1} to the west of the boundary as a result of surface heating. To the east of the boundary, low clouds inhibited surface heating.

Based on the synoptic precursors, forecasters at the Storm Prediction Center (SPC) forecasted a 5%–15% chance for severe hail (>2.5 cm) and wind (>25 m s^{-1}) and <2% chance for tornadoes within 40 km of a point in central New York in their morning and midday outlooks. Forecasters at the Albany National Weather Service office noted the possibility of isolated strong thunderstorms in their morning hazardous weather outlook. SPC mesoscale analyses from 1500 to 2100 UTC (Hart et al. 2015) had supercell parameters of 0.5–1.0, significant tornado parameters near zero, and significant hail parameters of 0.5–1.0 over the area in which the supercell traversed. Values for each parameter did not provide strong indications for the significant severe weather that would materialize (Thompson et al. 2003).
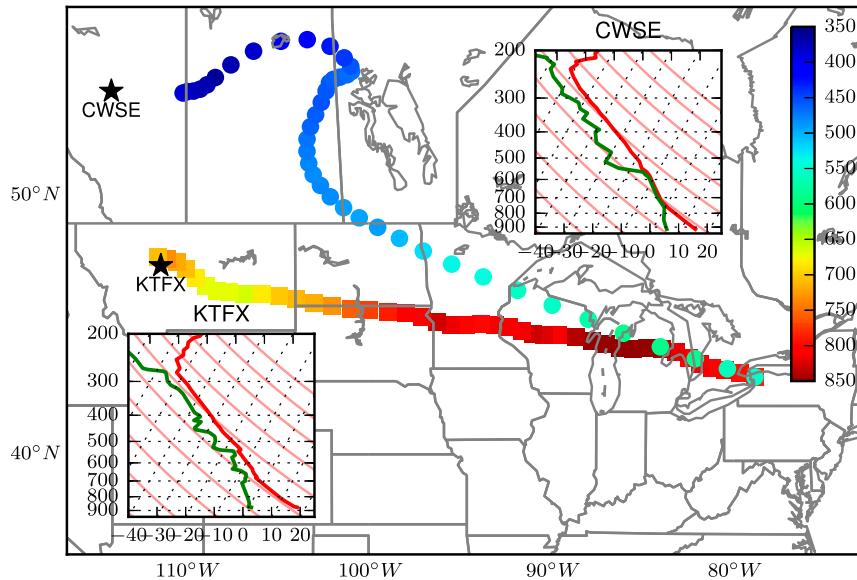
FIG. 6. The 3.5-day back trajectories initialized at 1200 UTC 22 May 2014 at Buffalo. The circles are the upper trajectory and the squares are the lower trajectory. Interval is 2 h between successive points. Color shading along the trajectory gives the parcel pressure level (hPa). The 0000 UTC 19 May 2014 soundings at KTFX and CWSE are shown in the insets.

WHAT MADE THIS EVENT UNEXPECTED FROM A PREDICTABILITY STANDPOINT?

The location was unexpected due to the background vertical wind shear. Global Forecast System (GFS) 1200 and 1800 UTC analyzed 0–6-km bulk shears were under $10 \, \mathrm{m \, s^{-1}}$ in the area where the cell initiated, 10–$15 \, \mathrm{m \, s^{-1}}$ in the southern Adirondacks, and 15–20 $\mathrm{m \, s^{-1}}$ in the Mohawk valley. The values north of the Mohawk valley were generally subcritical for idealized simulations of supercells in numerical models (Weisman and Klemp 1982). Yet, as seen in Fig. 2, the supercell was able to develop in this seemingly low-shear environment.

The severity was also unexpected. Synoptic features were generally weak, except for the EML. Much stronger upper-level troughs and deep surface cyclones characterized past significant tornado events (LaPenta et al. 2005; Bosart et al. 2006; Banacos et al. 2012). The record-tying hail, despite the EML, was unexpected. Although there was other convection, only one other severe hail report not associated with this storm occurred in the Albany county warning area, making this an isolated, significant severe event.

b. Origin of the EMLs

Since the EMLs were the strongest signal for severe weather in the synoptic picture and are a recurring ingredient in prior studies of severe weather in the Northeast, it is worthwhile to investigate their origin for this case.

The 1200 UTC Buffalo sounding served as a representative upstream sounding for the supercell environment. Given the northwesterly 10–20 $\mathrm{m \, s^{-1}}$ flow through both EMLs in the Buffalo sounding, it is likely that portions of both EMLs advected over the Adirondacks, Catskills, and Mohawk valley during the supercell time frame.

Figure 6 shows back trajectories originating from Buffalo using the NOAA Hybrid Single Particle Lagrangian Integrated Trajectory model with GFS data (Draxler and Rolph 2015). The back trajectory centered on the lower EML had a source region in the northern Rockies and plains. The 0000 UTC 19 May 2014 sounding from Great Falls, Montana (KTFX), had a deep mixed layer up to 675 hPa, and the 0000 UTC 20 May 2014 sounding from Bismarck, North Dakota, also had a similar mixed layer height (not shown). Westerly flow, combined with subsidence, preserved the character of the EML as it was advected eastward. Banacos and Ekster (2010) hypothesize that the combination of eastward advection and subsidence is important for the maintenance and transport of EMLs from the Intermountain West to the Northeast. The back trajectory centered on the higher EML had a source region in southern Canada above 400 hPa. The 0000 UTC 19 May 2014 sounding from Edmonton,

Alberta (CWSE), had steep lapse rates in the 450–300-hPa layer, associated with the cold air of an upper-level trough. This air quickly moved toward the southeast and subsided. The subsidence inversion below the base of the higher EML in the 1200 UTC Buffalo sounding was consistent with this pathway.

4. Initiation and early phase

The antecedent synoptic signal was ambiguous, but mesoscale inhomogeneities due to the terrain and boundary interactions with the storm appeared to be important at multiple stages of the storm evolution. We wish to emphasize that we are chiefly investigating aspects of the mesoscale environment just ahead of the supercell, and not the meso-γ-scale structure of the supercell itself. An investigation of the latter is not possible with the HRRR since it does not have a forecast run that maintains the supercell to a reasonable degree. Although the supercell is not well forecast, the mesoscale flow–terrain interactions and boundaries in the HRRR are all diagnostically useful.

The storm initiated near the intersection of two boundaries in the higher terrain of the Adirondacks shortly after 1515 UTC (Fig. 7b). The first boundary was an outflow boundary (solid green line in Figs. 8a,b) from a mesoscale convective system (MCS) that formed in Ontario overnight and moved eastward across northern New York (Fig. 7a). The second boundary was the aforementioned north–south baroclinic boundary (dashed green line in Figs. 8a,b) along the Hudson valley. A local maximum in low-level convergence at the intersection of the two boundaries, combined with lift ahead of the upper-level short-wave and orographic influences, likely aided in the initiation of the convection.

The cell tracked toward the south-southeast from 1600 to 1700 UTC (Figs. 7c–f). The mesoscale environment around the storm was characterized by surface equivalent potential temperatures around 320 K (Figs. 8c,e) and surface-based CAPE between 500 and 1000 J kg^{-1} (not shown), providing modest buoyancy to sustain the updraft.

The streamwise vorticity averaged through the lowest kilometer was above 5×10^{-3} s^{-1} (Figs. 8d,f) in the mesoscale environment around the storm. Storm-relative inflow parcels containing these values of streamwise vorticity could then contribute to the updraft rotation (Davies-Jones 1984). Additional streamwise vorticity may have been generated baroclinically in the forward flank of the supercell as it grew in extent (Rotunno and Klemp 1985).

The south-southeast motion was to the right of the shear vector (Fig. 9). One possible mechanism for the deviate motion is dynamic pressure perturbation gradients (Rotunno and Klemp 1985). A comparison of the Bunkers et al. (2014) storm motion with the observed storm motion suggests this possibility, although the observed storm motion is generally slower and not as far toward the east, especially from 1600 to 1700 UTC. Despite some weak rotation at both the lower and middle levels (Fig. 3), the cell also had multicellular characteristics before 1700 UTC. It is possible that the motion was influenced by factors other than supercell dynamic pressure perturbation gradients. Other possible mechanisms for the deviate motion include back-building either due to cold pool interactions with the higher terrain to the west of the track or a "zipper" effect between the two boundaries (Houston and Wilhelmson 2007, 2012). The zipper effect is the merging of two boundaries in the vicinity of a cell, allowing for updraft redevelopment and/or maintenance on the upstream flank of the cell.

Additionally, the south-southeast motion differed from nearby cells. Two nearby cells, denoted A and B in Figs. 7d, 7f, and 7h, initiated to the west and east of the supercell, respectively. Cell A was also located in the warm sector ahead of the outflow boundary. Cell B was located much farther into the cool side of the north–south baroclinic boundary. Both of these cells moved toward the southeast, were not characterized by any persistent rotation, and did not produce any severe weather reports. These characteristics were the same for all convection that formed north of the Mohawk valley. The comparison provides evidence that the large-scale environment north of the Mohawk valley was not conducive for widespread severe weather and that the localized mesoscale support for severe weather was important for this event.

After 1700 UTC, the cell met the criteria of a supercell, as the depth of the mesocyclone increased to >7 km in height, and both the low- and midlevel differential velocities of the mesocyclone increased to >20 m s^{-1} (Fig. 3). The HRRR-analyzed 0–6-km bulk shear in the environment ahead of the supercell was 12 m s^{-1} at 1700 UTC (Fig. 9). As noted earlier, 12 m s^{-1} is subcritical for supercells in idealized homogeneous simulations (Weisman and Klemp 1982).

Shear variations due to analysis errors or poorly represented mesoscale inhomogeneities due either to resolution deficiencies or lack of observed data may be important to consider. One possible mesoscale inhomogeneity may have been a band of locally higher 0–6-km shear due to the superposition of the westerly midlevel flow associated with the remnant vortex of the
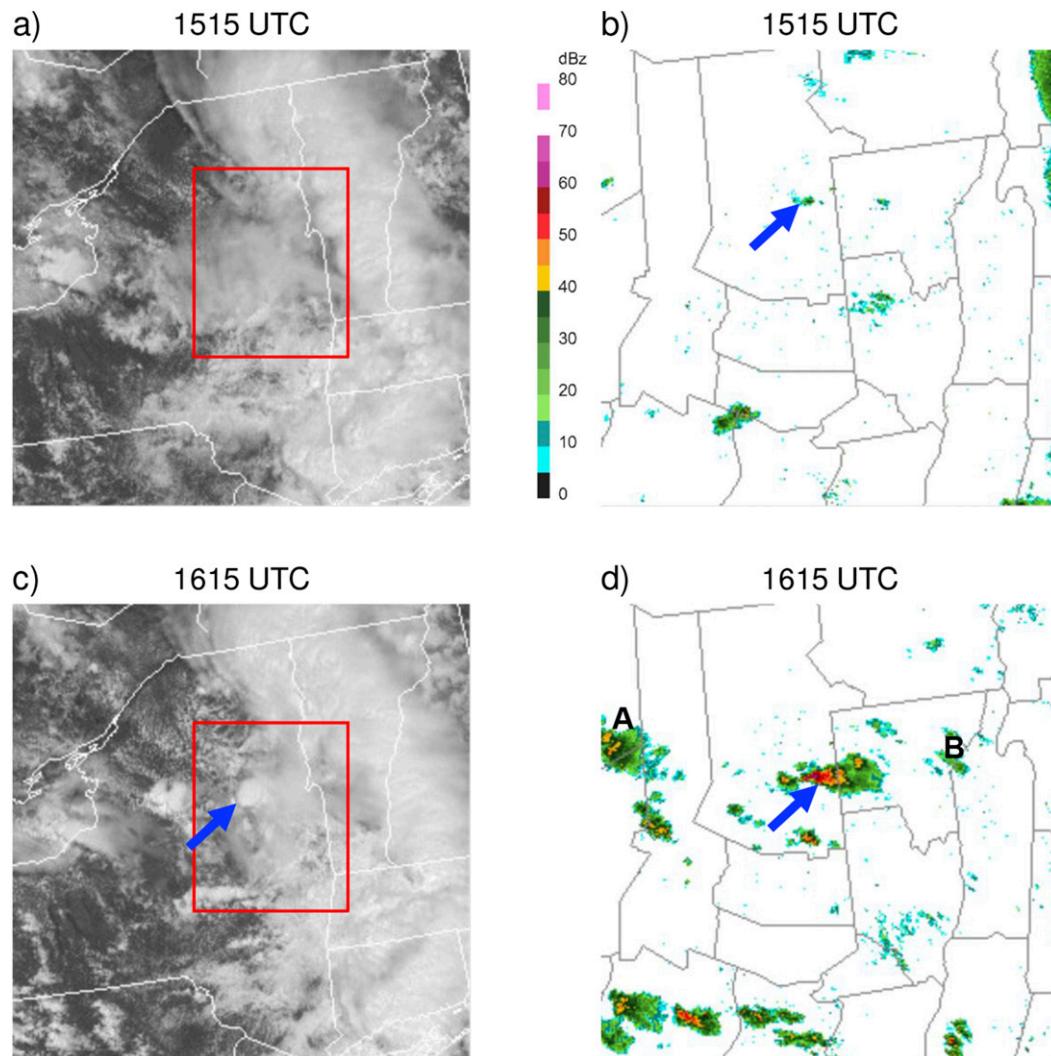
FIG. 7. *GOES-13* visible satellite imagery and KENX 0.5°-elevation reflectivity at (a),(b) 1515, (c),(d) 1615, (e),(f) 1715, (g),(h) 1815, and (i),(j) 1915 UTC 22 May 2014. The red box gives the radar domain and the domain in Fig. 8. The blue arrow points to the supercell. Other cells are annotated with letters.

MCS and the synoptic-scale flow (Trier and Davis 2007). Additionally, there existed a strong north–south gradient of 0–6-km bulk shear, and small shifts or undulations in the orientation of the gradient might have made a big difference in the storm environment. The 0–6-km bulk shear was supportive for supercells just south of the Mohawk valley. A splitting supercell, C in Figs. 7f, 7h, and 7j, was observed between 1700 and 1900 UTC. Other supercells were observed farther south over the Catskills. However, there was no direct observational evidence to suggest errors in the HRRR or GFS winds that would cause the shear to be greater than analyzed north of the Mohawk valley. Additionally, none of the convection to the north of the Mohawk valley, save the cell being discussed, showed supercell characteristics.

Overcast conditions in the maritime air persisted in the Hudson valley, while clearing occurred to the west (Fig. 7, left). The strong surface heating and weak synoptic forcing from the short wave caused surface pressures to drop west of the boundary (Figs. 8a,c,e), resulting in an increasing surface pressure gradient across the Hudson valley. As a result, the surface winds in the Hudson valley backed in direction and intensified.

The backing winds can be inferred from the change in direction of the 0–1-km storm-relative winds between 1700 and 1800 UTC (Figs. 8f,h). The storm-relative winds intersecting the storm prior to 1700 UTC were southwesterly but changed to southeasterly at 1800 UTC, as the storm began to move off the Adirondacks. The change in direction may have been timely for the
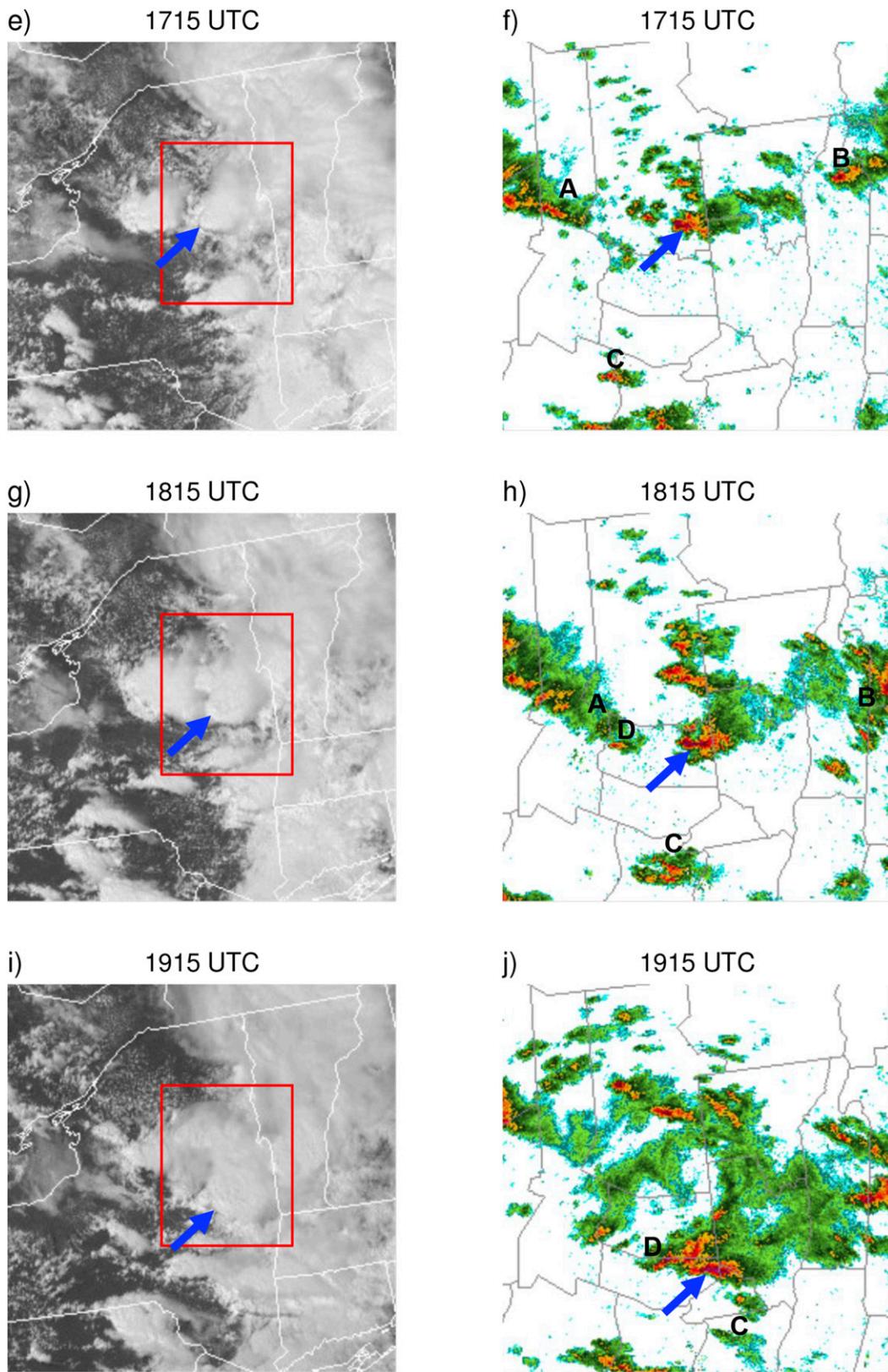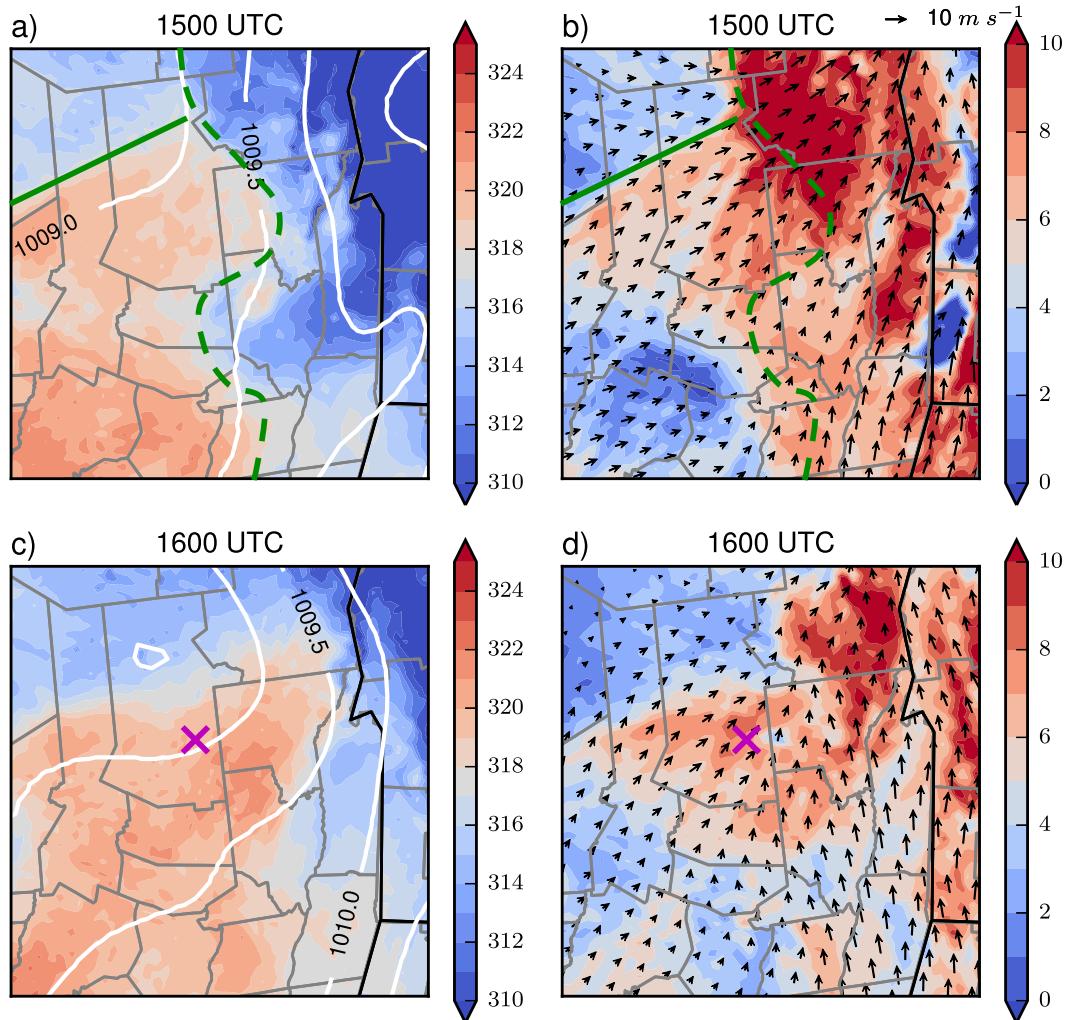
FIG. 7. (*Continued*)

FIG. 8. HRRR analyses at (a),(b) 1500, (c),(d) 1600, (e),(f) 1700, (g),(h) 1800, and (i),(j) 1900 UTC. (left) Surface equivalent potential temperature (shading; K) and mean sea level pressure (white contours; interval is 0.5 hPa). (right) Streamwise vorticity (shading; $10^{-3}\,s^{-1}$) averaged through the lowest kilometer and storm-relative winds (vectors; m s^{-1}) averaged through the lowest kilometer. The purple $\times$ gives the location of the supercell. In (a) and (b), the outflow boundary (solid green line) and north–south baroclinic boundary (dashed green line) are drawn.

supercell because the streamwise vorticity to the southeast increased as a result of the increasing surface baroclinicity along the boundary, while the streamwise vorticity dwindled to the southwest (Fig. 8h).

The backing of the winds up the Hudson valley also enhanced upslope flow on the southeast slope of the Adirondacks adjacent to the Hudson and Mohawk valleys. Figure 10a shows the upslope component of the flow, given by $\mathbf{v} \cdot \nabla z_0$, where $\mathbf{v}$ is the near-surface horizontal wind velocity and z_0 is the elevation. A local maximum of $0.24\,m\,s^{-1}$ of upslope flow was analyzed just ahead of the supercell at 1800 UTC. The supercell passed over the region of upslope flow between 1810 and 1820 UTC. Over the subsequent 20 min, both the low- and midlevel mesocyclone differential velocities increased 15 m s^{-1} (Fig. 3).

The upslope flow was associated with increasing moisture in the lower troposphere. Figure 10b shows time series of the upslope flow and the 850-hPa relative humidity at the location of the maximum upslope in Fig. 10a. The 850-hPa relative humidity increased from 65% to saturation from 1500 to 1800 UTC before the cell passed over the location. Granted, the largest increase in upslope flow occurred from 1700 to 1800 UTC because of the backing winds. The increase in lower-troposphere relative humidity and the intensification of the cell as it crossed over the area of upslope is consistent with the idealized study of Markowski and Dotzek (2011), which had upslope flow magnitudes around $0.1\,m\,s^{-1}$. However, the time-evolving environment and other factors may have also played a role in intensifying the supercell between 1800 and 1900 UTC.
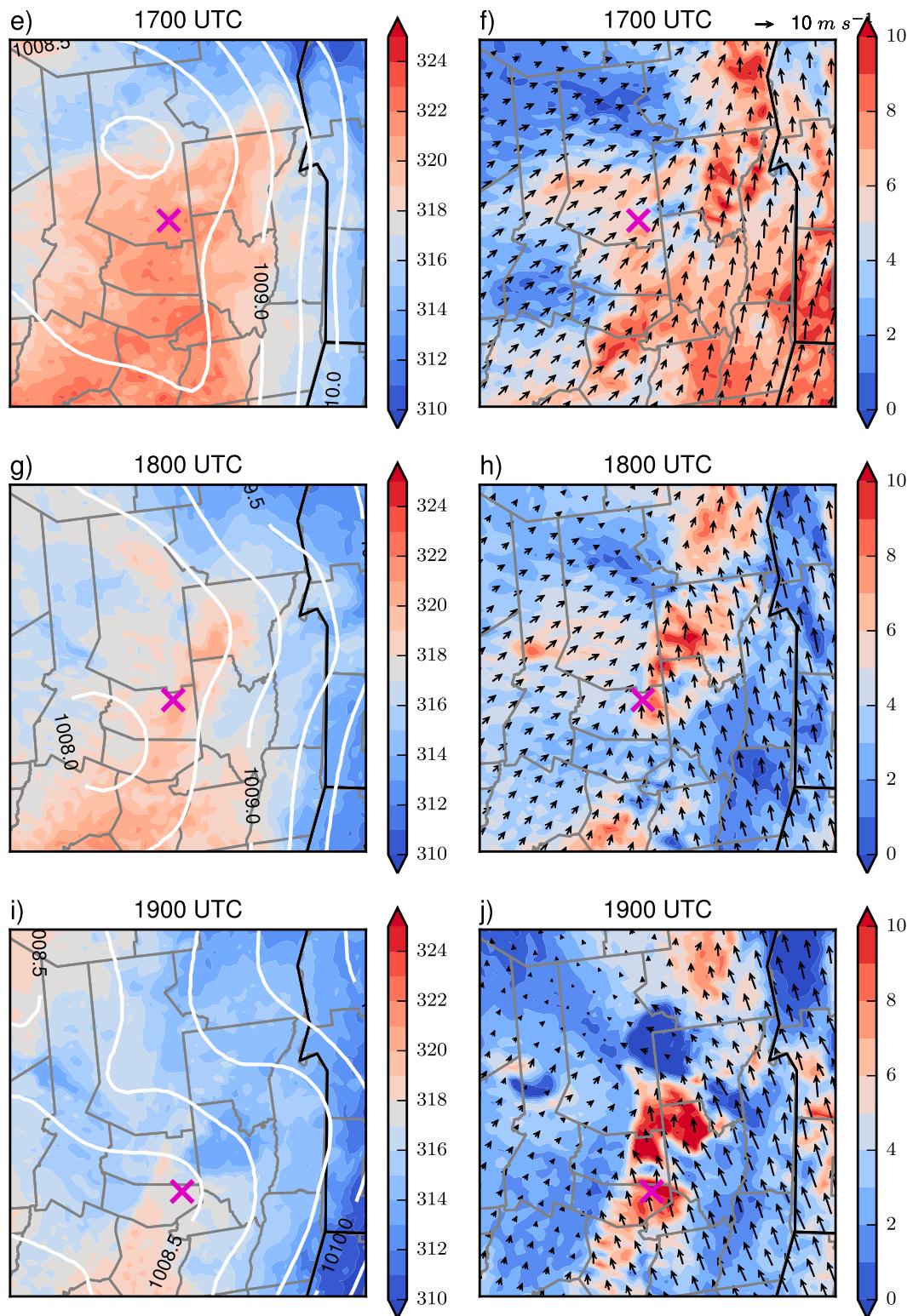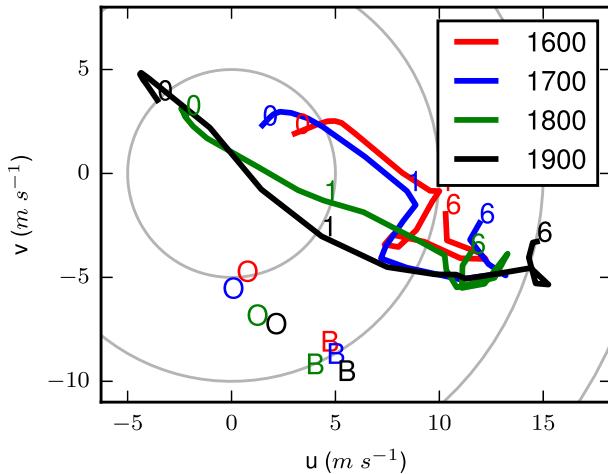
FIG. 8. (*Continued*)

FIG. 9. The 1600–1900 UTC HRRR hodographs in the pre-convective environment 30 min ahead of the supercell. The labels 0, 1, and 6 in the hodograph are the heights above ground level. The B shows the Bunkers et al. (2014) storm motion for a right-moving supercell. The O is the observed average storm motion in the subsequent hour.

5. Severe phase

The largest impacts occurred between 1800 and 2000 UTC. We first examine lightning and radar observations of the storm to document this highly anomalous event for the Northeast and then provide evidence for how mesoscale factors contributed to the severity of the storm.

a. Lightning and radar observations

Sudden increases in lightning flashes, or a lightning jump, can signal an enhanced risk of severe weather (e.g., Chronis et al. 2015). Schultz et al. (2009) define a lightning jump to occur when lightning flashes for a particular storm increase by more than two standard deviations from the prior 10 min of lightning flash frequencies. Although CG lightning is a small fraction of the total lightning, Schultz et al. (2011) find that CG lightning jumps can precede or be coincident with severe weather reports. A CG lightning jump occurred at 1830 UTC (Fig. 3), 10 min after the intersection with the area of upslope flow and coincident with the first severe hail report.

The lightning jump also marked a change in the radar presentation of the supercell. Maximum vertically integrated liquid values increased from a time average of 50 kg m^{-2} in the three scans before 1830 UTC to 74 kg m^{-2} in the three scans after 1830 UTC. The 60-dBZ echo-top height doubled from 4.5 to 9.0 km, indicating increased updraft strength and storm depth (not shown).

After 1840 UTC, CG flash rates suddenly dropped. Subsequently, CG flash rates did not exceed 5 flashes $(4 \text{ min})^{-1}$ until 1945 UTC, when another lightning jump occurred. Between 1840 and 1945 UTC, an additional 19 severe hail reports, including the 10-cm hailstone, were received.

Severe hail-bearing storms are observed to have low CG flash rates (Lang et al. 2000; Soula et al. 2004). The reduced flash rates may be caused by strong updrafts lofting negatively charged particles higher into the cloud, enhancing intracloud flashes at the expense of CG flashes (MacGorman et al. 1989). Wet hail growth also inhibits electrification by charge exchange (Saunders
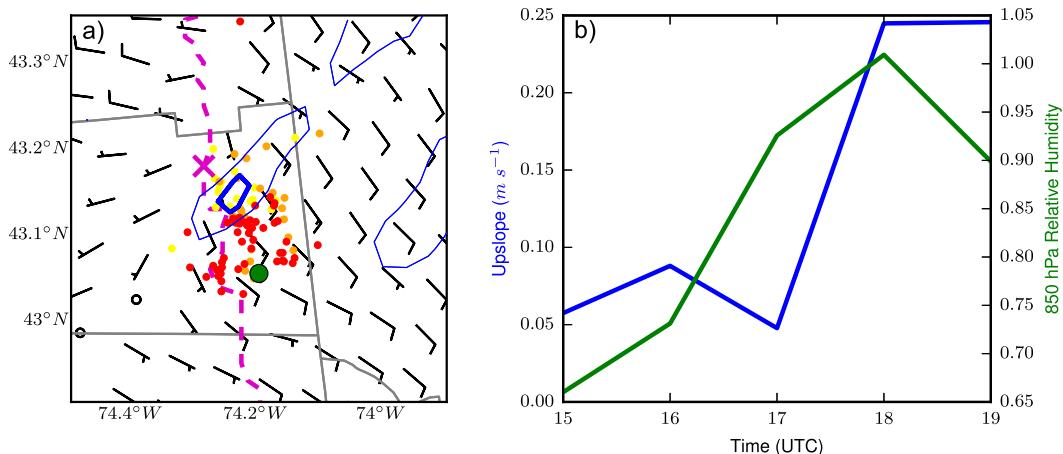

FIG. 10. (a) HRRR 1800 UTC analyzed 80-m winds (barbs; m s^{-1}) and upslope flow (thin blue contour, 0.1 m s^{-1}; thick blue contour, 0.2 m s^{-1}). NLDN CG lightning flashes between 1810 and 1820, 1820 and 1830, and 1830 and 1840 UTC are given by the yellow, orange, and red dots, respectively. The track of the mesocyclone is given by the purple, dashed line, and the location of the mesocyclone at 1800 UTC is given by the ×. The first severe hail report at 1830 UTC is given by the green dot. (b) The 1500–1900 UTC HRRR-analyzed upslope flow (blue) and 850-hPa relative humidity (green) at the 1800 UTC maximum upslope flow location.
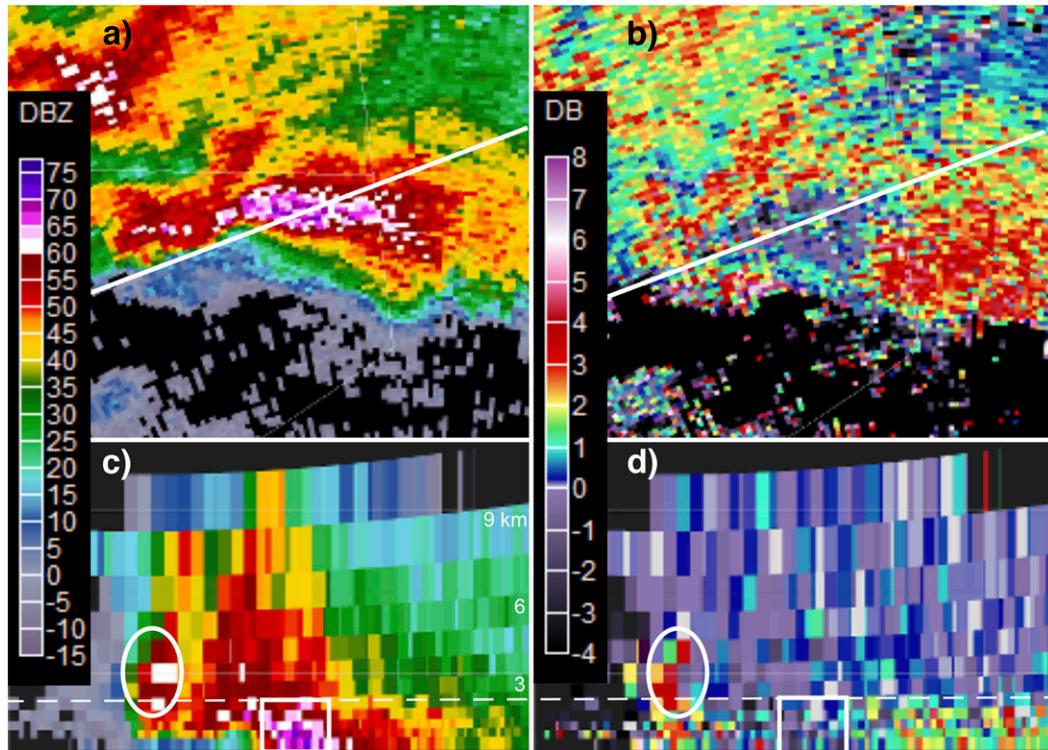
FIG. 11. The KENX 1905 UTC 0.5°-elevation (a) reflectivity (dBZ) and (b) differential reflectivity (dB). The white line gives the vertical cross sections shown in (c) and (d) for each respective product. The dashed white line is the HRRR-estimated wet-bulb zero level. The oval demarcates the Z_{DR} column, and the rectangle demarcates the large-hail core.

and Brooks 1992; Emersic et al. 2011). A full diagnosis of the total lightning behavior due to the charging evolution of the cloud is beyond the scope of this study.

Dual-polarization products between 1900 and 1925 UTC from the KENX radar also provided evidence for supercooled water and wet hail growth. For example at 1905 UTC, a prominent differential reflectivity Z_{DR} column (Conway and Zrni 1993) extended to 5.5 km above ground level (Fig. 11d). The Z_{DR} values were greater than 3 dB and coincided with reflectivities around 50 dBZ (Fig. 11c). Additionally, a specific differential phase K_{DP} column extended to 4 km above ground level, where values were $2°$–$4° km^{-1}$ (not shown). Correlation coefficients were 0.90–0.93 within the Z_{DR} and K_{DP} columns, indicative of a mixture of hydrometeors (not shown). HRRR-estimated wet-bulb temperatures were approximately $-10°$ and $-20°C$ at the K_{DP} and Z_{DR} column tops, respectively (Lee 2015). Three-body scatter spikes (Lemon 1998) appeared at several times, but were largely obscured by a large area of rain to the north of the supercell. These radar signatures together provided strong evidence for significant wet hail growth in the hail growth layer (Kumjian and Ryzhkov 2008).

Farther east on the forward flank of the storm, there was a strong radar signature for large hail. Figures 11a and 11c show the reflectivities exceeded 70 dBZ in the low-elevation radar scans below the freezing level, around the time when the 5–10-cm hail was reported. The highest reflectivities were coincident with an area of near-zero and negative Z_{DR}, as seen in Figs. 11b and 11d. Volume scans indicated the high reflectivity and low Z_{DR} values extended well past 9 km above ground level, an indication of a stout hail core and powerful updrafts (not shown).

Ryzhkov et al. (2013b) developed a polarimetric-based categorical hail-size algorithm. One of the key distinguishing features between giant hail greater than 5 cm and smaller hail is the Z_{DR} signature below the melting level. Smaller melting hail has higher Z_{DR} values, similar to large raindrops, whereas larger melting hail retains low Z_{DR} values all the way to the surface (Ryzhkov et al. 2013a). The 1800 UTC HRRR melting level across Amsterdam was 2.3 km above ground level. The Z_{DR} values remain near zero from the melting level to the lowest scan level at about 0.8 km above ground level (Fig. 11d). These patterns support the presence of giant hail below the melting level. The giant hail was observed through 1925 UTC, except for one additional 7.5-cm hail report at 2000 UTC in Duanesburg that was preceded by radar signatures similar to those that occurred over Amsterdam.
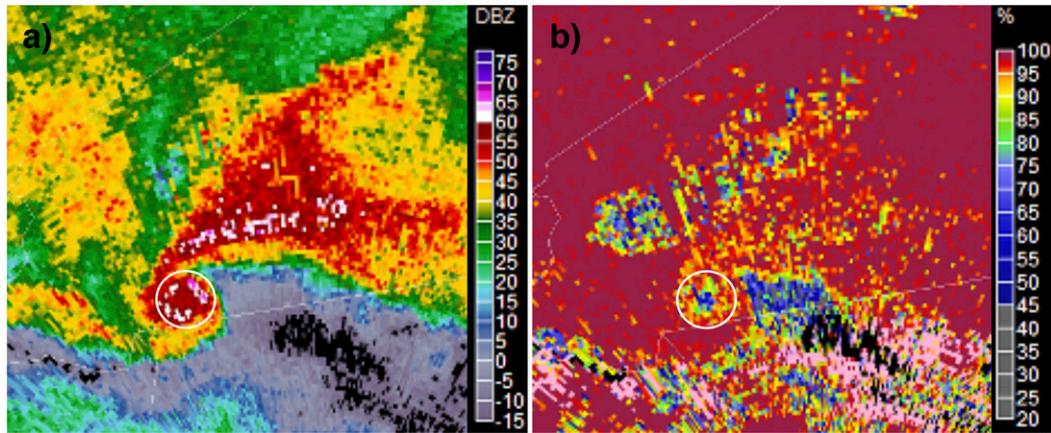
FIG. 12. The KENX 1951 UTC 0.5°-elevation (a) reflectivity (dBZ) and (b) correlation coefficient (%). The debris ball is circled.

Beginning around 1920 UTC, the tornadic phase of the supercell began. Tornadogenesis occurred during a local minimum in CG flashes. In fact, there was only one detected flash in the 8 min preceding tornadogenesis. This reduction in CG flashes just before tornadogenesis has also been observed in other case studies of tornadoes (Seimon 1993; Steiger et al. 2007). Perez et al. (1997) conducted a statistical study of lightning behavior associated with violent tornadoes. Their data also indicate there is a signal for decreasing CG flash rates leading up to tornadogenesis, with 48% of the cases having a minimum in CG flash rates at the time of tornadogenesis.

The radar signatures leading up to tornadogenesis were complex and evolved rapidly. A nonsevere cell, denoted D in Figs. 7h and 7j, merged with the western flank of the supercell at 1923 UTC. Lee et al. (2006) find that mergers are associated with increased supercell rotation. During one particular outbreak, 54% of the tornadoes formed within 15 min of mergers. Wurman et al. (2007) hypothesize that increased low-level convergence during the merger may enhance or cause tornadogenesis. The low-level mesocyclone started to quickly intensify at 1928 UTC (Fig. 3). The first tornado damage was at 1933 UTC, 10 min after the merger.

At the peak intensity of the tornado between 1947 and 1951 UTC, a tornadic debris ball signature was evident (Fig. 12). Correlation coefficients were 0.6–0.8 within the center of the hook echo. Low correlation coefficients extended up to 3.5 km above ground level, signaling the lofting of debris. Convection along the inferred rear-flank downdraft appeared as a leading arc of >40-dBZ echoes extending from the east side of the hook echo back toward the west. Soon after, the arc of convection

surged toward the southeast, and the tornado finally dissipated at 1955 UTC.

b. Role of terrain and boundary

Terrain channeling and convergence along the boundary are hypothesized to have played an important role in the large hail formation by enhancing the instability in the Mohawk valley. Figure 13 shows the mean sea level pressure data from Albany (KALB); Schenectady, New York (KSCH); and Johnstown, New York (KNY0). The locations of the three stations are shown in Fig. 2. These three stations are oriented from southeast to northwest up the Mohawk valley. The supercell itself passed between KSCH and KNY0 at 1900 UTC, so the stations are useful for examining pressure differences and changes in flow up the Mohawk valley in the several hours preceding the supercell passage.

Before 1600 UTC, the mean sea level pressures at all three stations were just above 1009 hPa. After 1600 UTC, differences began to arise, especially between KNY0 and the other two surface stations. KNY0 dropped from 1009.2 hPa to a minimum of 1006.7 hPa at 1830 UTC, while KALB and KSCH only dropped to 1008.5–1009 hPa during the same time interval. The drop in mean sea level pressure at KNY0 may be attributed to a combination of synoptic-scale forcing with the approaching short wave and stronger surface heating at and west of KNY0, although some of the pressure falls very close to 1830 UTC may be caused by the pressure perturbations of the supercell itself. Sky conditions remained overcast at both KALB and KSCH, where temperatures remained steady around 18°C. Temperatures rose from 16° to 20°C at KNY0 as a result of some breaks in the overcast. Temperatures were likely higher just to the west of KNY0 where there was more sunshine. Citizen Weather
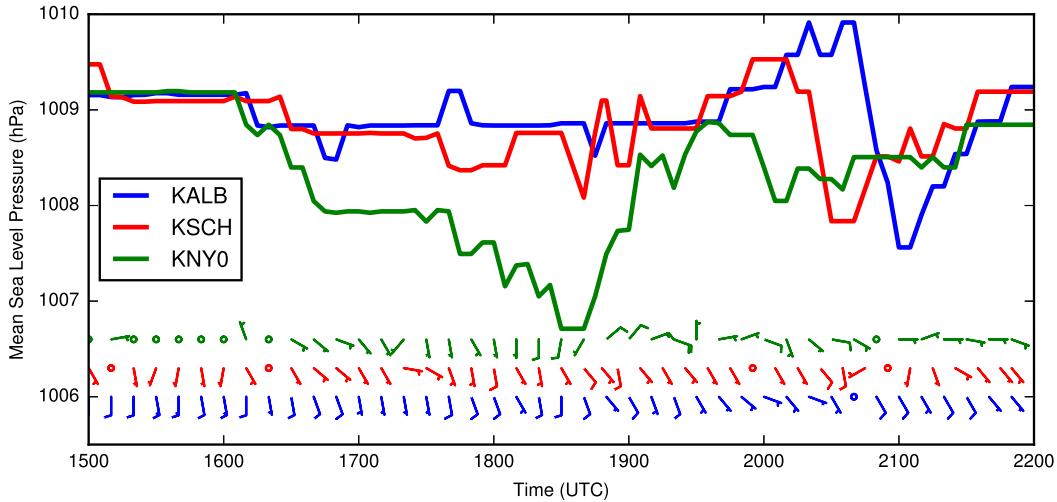
FIG. 13. Time series of mean sea level pressure (hPa) from KALB (blue), KSCH (red), and KNY0 (green). Colored barbs give the wind velocity (m s^{-1}) for each station every 20 min.

Observer Program (Chadwick 2015) stations 20–40 km west of KNY0 recorded temperatures between 22° and 24.5°C at 1830 UTC. The pressure drop at KNY0 was consistent with what would be expected from a hydrostatic balance adjustment due to the observed temperature change, assuming the thermal and mass profiles above the boundary layer were steady.

The maximum pressure difference between KNY0 and KALB was about 2 hPa at 1830 UTC over the distance of 50 km separating the two stations. The increasing pressure gradient up the Mohawk valley induced an ageostrophic flow that caused the winds to slightly back at KSCH and KALB between 1500 and 1900 UTC. For example at KSCH, the mean wind was 175° at 2 m s^{-1} between 1500 and 1600 UTC and 150° at 3.5 m s^{-1} between 1800 and 1900 UTC. Differences in both the wind speed and direction at KSCH during the two time intervals are statistically significant using a rank-sum test.

The increasing alignment and strengthening of the flow along the Mohawk valley yielded greater moisture fluxes from the Hudson to Mohawk valleys. Figure 14 shows a north–south cross section of the 1800 UTC HRRR moisture flux. The cross section is centered at the 1900 UTC position of the supercell. Negative values indicate a moisture flux toward the west. The largest moisture fluxes were in the Mohawk valley, particularly in the lowlands just north of the Mohawk River. Additionally, the moisture flux up the valley was shallow, confined below 0.9 km in height.

The largest changes in moisture flux from 1500 to 1800 UTC also occurred in the Mohawk valley. At 1500 UTC, negative moisture fluxes were confined below 0.5 km in height and relatively weak. By 1800 UTC,

negative moisture fluxes roughly doubled in depth and increased in magnitude by 10–40 m s^{-1} g kg^{-1}. The largest increases were in the Mohawk valley, where the flow was channeled. Because of the significant biases in the HRRR surface dewpoints, which will be detailed shortly, the low-level moisture flux in the Mohawk valley was likely underestimated.

The flow up the Mohawk valley slowed as it continued westward and approached the boundary. Froude numbers at 1800 UTC, calculated using HRRR data at KSCH, were supercritical (>1) for depths less than
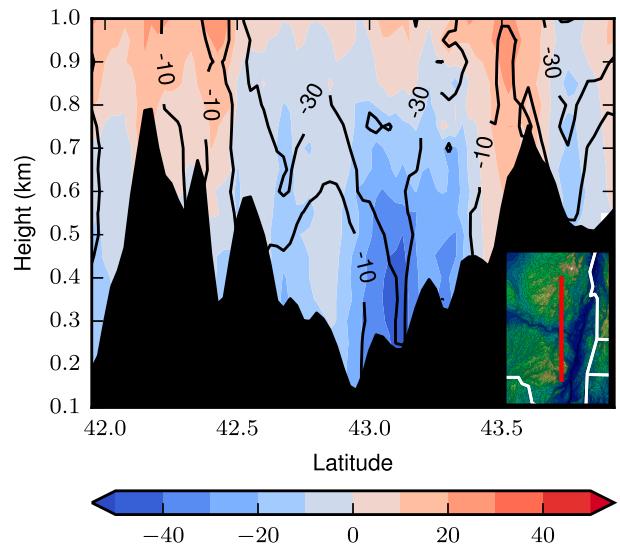

FIG. 14. Cross section of the 1800 UTC HRRR zonal moisture flux (shaded; m s^{-1} g kg^{-1}) along the red line given in the inset. Contours give the 3-h change from 1500 to 1800 UTC in the moisture flux. The black area is the topography along the cross section.
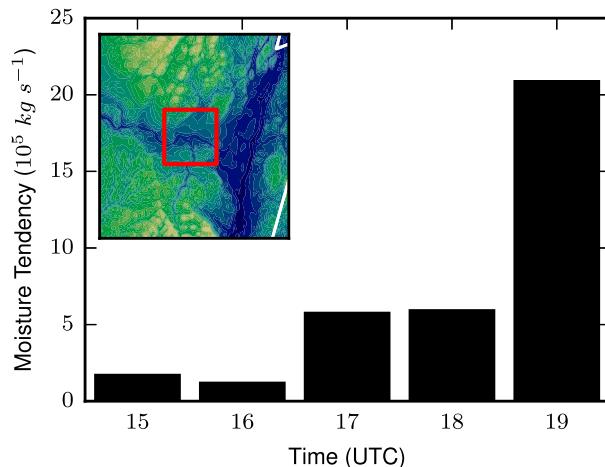
FIG. 15. HRRR hourly moisture tendency (10^5 kg s^{-1}) due to the integrated horizontal moisture flux convergence in the red box given in the inset.

500 m and subcritical (<1) for depths greater than 500 m, indicating that the cool, moist air would be able to spread up the Mohawk River and adjacent lowlands all the way west to the boundary, but would be blocked by the higher terrain of the Catskills and Adirondacks. Along and to the east of this boundary in the Mohawk valley, the horizontal moisture flux convergence was maximized. Figure 15 shows the integrated horizontal moisture flux convergence, or moisture tendency, in the 1-km-deep box in the figure inset. The moisture tendency was relatively weak at 1500 and 1600 UTC, but increased significantly at 1700 UTC, as the moisture flux at the eastern end of the valley increased. At 1900 UTC, the moisture tendency was maximized because of strong low-level convergence, likely reflecting the low-level convergence of the HRRR-represented convection itself. Nevertheless, there was an increasing tendency for the low-level horizontal flow to increase the low-level moisture in the eastern Mohawk valley a couple hours in advance of the supercell entering the valley.

The maximum instability existed where the horizontal moisture flux convergence overlapped with the warmer temperatures because of surface insolation. Figure 16 shows two surface-based CAPE calculations. The panel on the left is the direct calculation from the 1800 UTC HRRR analysis, and the panel on the right substitutes the 1800 UTC Real-Time Mesoscale Analysis (RTMA; De Pondeca et al. 2011) surface temperature and dewpoint values in place of the HRRR values and recalculates the CAPE. There are significant differences in the two analyses. The HRRR had a broad area of 500–1000 J kg^{-1} of CAPE with small patches of >1000 J kg^{-1} along the surface wind convergence boundary where the surface southeasterlies and westerlies meet. On the

other hand, the RTMA-modified CAPE had a local area of 2000–2500 J kg^{-1} in the Mohawk valley and isolated areas of >2500 J kg^{-1} right along the Mohawk River. CAPE differences in the two analyses were largely due to differences in surface dewpoint temperatures. The HRRR had dewpoint temperatures 3°–6°C lower than the RTMA in the Mohawk valley. The 1800 UTC KNY0 dewpoint observation supported the HRRR low bias, with an error of −4°C. Therefore, the RTMA-modified CAPE values are more believable in the Mohawk valley. The low moisture bias is a known pattern in the version of the HRRR used at the time (J. Kenyon 2014, personal communication).

Figure 17a shows a 1700 UTC HRRR sounding along the Mohawk River near the location of the large hail reports that would occur 2 h later. An EML existed between 800 and 700 hPa, representing the earlier EML sampled in the 1200 UTC Albany and Buffalo soundings. The warm nose at 800 hPa provided a weak cap, allowing the horizontal moisture flux convergence to increase the moisture below the cap. While there is no distinct higher EML as was observed in the 1200 UTC Buffalo sounding, lapse rates in the 600–400-hPa layer were 8.0°C km^{-1}. The higher EML may have been modified by convection over central New York earlier in the day or may not be well represented. Regardless of the EML structure, freezing levels were anomalously low and midlevel lapse rates were anomalously high for this date. Additionally, this area was at the edge of 0–6-km shear values >15 m s^{-1} that were more supportive of supercells.

Figure 17b continues to indicate a remnant EML and an eroding warm nose at 800 hPa. The coldest air in the middle to upper levels moved overhead at this time. The RTMA-modified sounding had a lifted index of −8°C and a CAPE of 2200 J kg^{-1}, of which a substantial portion was located in the hail growth zone. The combination of the mesocyclone rotation, steep midlevel lapse rates provided by the EML, increasing instability due to the overlap of the terrain-influenced moisture flux convergence along the boundary and surface insolation, and sufficient deep-layer shear created conditions ripe for the large hail in the Mohawk valley (Johnson and Sugden 2014).

The backing and intensification of the surface winds just east of the boundary, as seen in Fig. 17, also affected the vertical wind shear. Changes in the wind shear were particularly pronounced in lower levels, where surface southeasterlies undercut westerlies at 1 km in height and lengthened the hodograph toward the upper left at 1800 and 1900 UTC (Fig. 9). Figure 18a shows the 0–1-km vertical wind shear at 1900 UTC. The vertical wind shear was enhanced along the boundary, particularly on the cool side near the intersection of the instability gradient
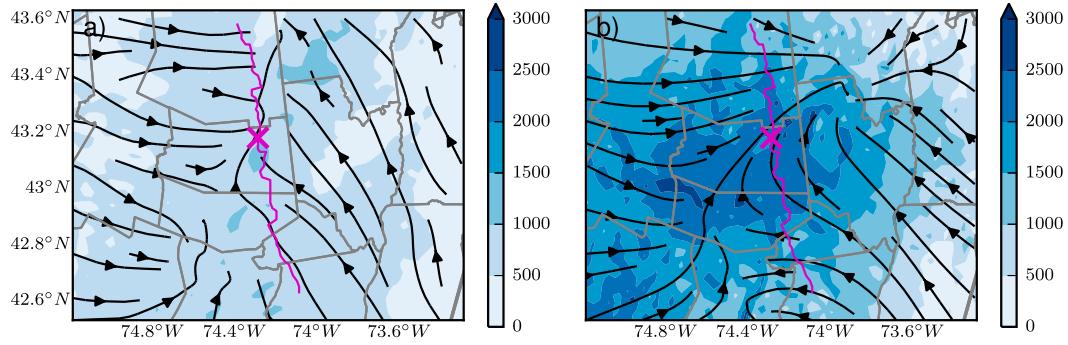
FIG. 16. (a) The 1800 UTC HRRR surface-based CAPE (J kg^{-1}) and surface streamlines. (b) The 1800 UTC RTMA-modified surface-based CAPE (see text for details) and surface streamlines. The mesocyclone track and 1800 UTC position are given by the purple line and the ×.

and the supercell track on the south side of the Mohawk valley (Fig. 16b). Here, 0–1-km shear magnitudes were at or above 10 m s^{-1}, near the median 0–1-km shear in proximity soundings for other significant tornado events (Thompson et al. 2003).

The strong low-level vertical wind shear implied large horizontal vorticity magnitudes. The close alignment of the horizontal vorticity and storm-relative flow vectors in the lowest kilometer implied large amounts of streamwise vorticity to the south of the supercell (Fig. 8j). The streamwise vorticity averaged through the lowest kilometer was 0.8–1.0 × 10^{-2} s^{-1} at 10–20 km ahead of the supercell along the cool side of the boundary. Maximum streamwise vorticity values near the surface were 1.5–2.0 × 10^{-2} s^{-1}. Both the lowest kilometer average and maximum streamwise vorticity values are comparable

with proximity sounding values for other significant tornado events (Markowski et al. 2003).

The 0–1-km storm-relative helicity was generally between 50 and 100 m^2 s^{-2} ahead of the supercell (Fig. 18b), because of the storm motion well off a mostly straight hodograph (Fig. 9). Although such values are below the 25th percentile for other significant tornado events, Thompson et al. (2003) find they typically occur in association with high boundary layer relative humidity and low lifting condensation levels. The RTMA-modified lifting condensation levels were about 400–600 m above ground level ahead of the supercell (not shown).

Low lifting condensation levels are hypothesized to be important for tornadogenesis because the rear-flank downdrafts in such environments potentially produce less dense cold pools and are conducive for tornadogenesis
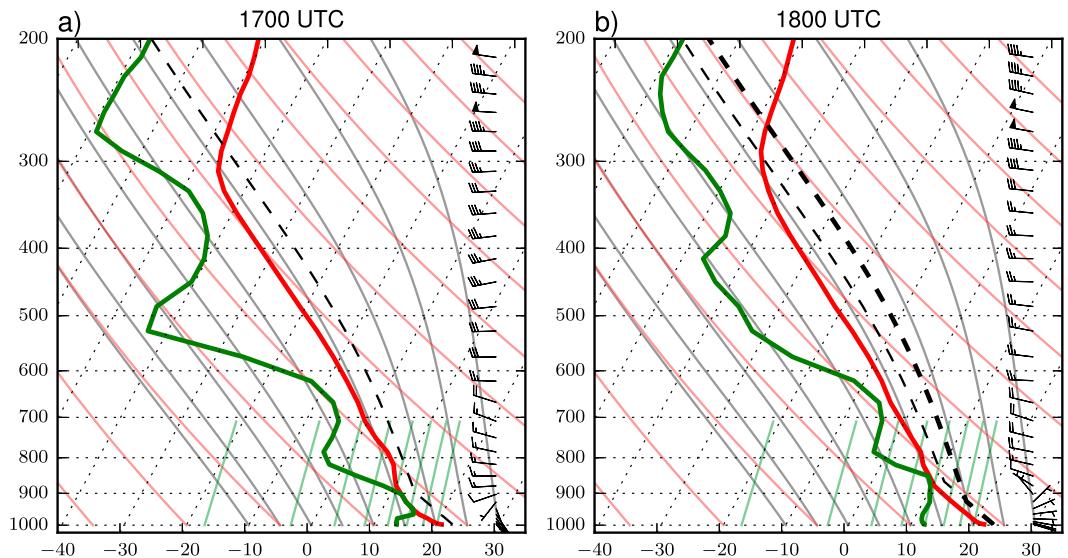

FIG. 17. HRRR analysis soundings at (a) 1700 and (b) 1800 UTC along the Mohawk River at the 1900 UTC location of the supercell. Thin dashed lines represent the surface parcel ascent from the HRRR, and the thick dashed line in (b) represents the RTMA-modified surface parcel ascent.
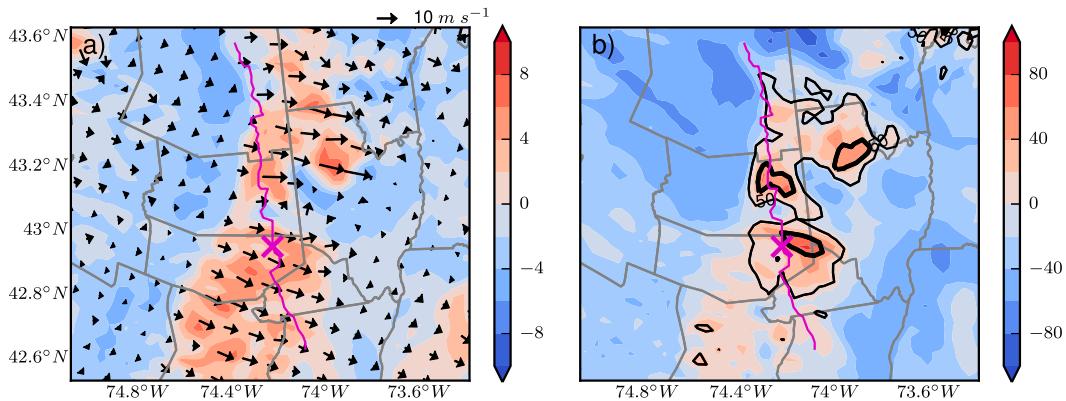
FIG. 18. The 1900 UTC HRRR (a) 0–1-km vertical wind shear vector (m s^{-1}) and (b) 0–1-km storm-relative helicity (thin contour, 50 m^2 s^{-2}; thick contour, 100 m^2 s^{-2}). Shaded fields are 3-h changes from 1600 to 1900 UTC of the vertical wind shear magnitude and storm-relative helicity. The mesocyclone track and 1900 UTC position are given by the purple line and the ×.

(Rasmussen and Blanchard 1998; Markowski et al. 2002). To estimate the strength of the cold pool, data were used from a Citizen Weather Observer Program station (CW9865) located about 5 km south of where the first tornado damage occurred. Radar data indicated the station was in the hook echo at 1942 UTC and thus provided potentially valuable information regarding the thermodynamic characteristics in the hook-echo region, with the caveat that the reliability of the station was unknown.

Following the methodology of Markowski et al. (2002), the virtual potential temperature perturbation was estimated to be the change in virtual potential temperature between the 1942 UTC observation and the 1827–1927 UTC average. The latter was an approximation for the base state, since the virtual potential temperature varied little over the hour ahead of the passage of the supercell. Liquid water effects on the virtual potential temperature were included, using the 0.5°-elevation reflectivity at CW9865 (Rutledge and Hobbs 1984). Virtual potential temperature perturbations were estimated to be between −3 and −5 K in the hook-echo region of the supercell, which was consistent with the "weakly tornadic" category in Markowski et al. (2002).

In summary, the combination of a narrow, but strong zone of 0–1-km wind shear, large values of streamwise vorticity, and low lifting condensation levels are hypothesized to have created conditions favorable for the EF3 tornado as the supercell crossed the boundary to the cool side.

6. Conclusions

The 22 May 2014 Duanesburg supercell was an unexpected event in terms of its location and severity. The storm produced 10-cm hail, tying the New York State record, and EF3 tornado damage. Unlike previous events in the literature documenting significant tornadoes in the Northeast, there was a lack of a strong upstream trough and a deep surface cyclone that would favor a regional severe weather outbreak. Indeed, the isolated nature of the event indicated synoptic-scale conditions did not favor widespread severe weather, especially so far north where the deep-layer shear was relatively weak. One key synoptic-scale feature was the presence of two EMLs and associated steep midlevel lapse rates and low freezing levels, a signal for severe hail events in the Northeast and tornadoes during 500-hPa northwesterly flow regimes, albeit rare (Johns and Dorr 1996; Hurlbut and Cohen 2014).

We hypothesize that the mesoscale details are what made this supercell special, affected by the interaction of the storm with the terrain and baroclinic boundaries. Initiation occurred at the intersection between an outflow boundary from an MCS and a north–south baroclinic boundary oriented along the Hudson valley. The cell was able to transition from a multicell to a supercell as it moved southward from the weaker to stronger environmental shear. The deviate motion to the right of the mean wind allowed the supercell to track roughly parallel to the north–south boundary. This track allowed the supercell to ingest buoyant air near the boundary to sustain its updraft, but also to stay in an environment with sufficiently high values of low-level streamwise vorticity in the vicinity of the two boundaries (Atkins et al. 1999).

The north–south boundary was anchored and strengthened by differential heating. Low clouds and a maritime air mass remained in the Hudson valley, while surface heating occurred in the Adirondacks, Catskills,

and Mohawk valley. The differential heating contributed to strengthening the zonal pressure gradient across the boundary, causing the winds to slightly back to a more easterly direction and strengthen in the Hudson and eastern Mohawk valleys.

The backing and strengthening of the winds, and their subsequent interaction with terrain, had several potentially important effects on the supercell evolution. First, it produced greater upslope flow along the southeastern Adirondack slopes. Upon the supercell intersecting a local maximum in the upslope flow, there was an intensification of the supercell mesocyclone and a lightning jump. Severe hail occurred during and after the lightning jump. Second, the low-level moisture flux was maximized at the eastern end of the Mohawk valley as a result of terrain channeling. The terrain channeling and the surface wind convergence boundary farther west led to increased horizontal moisture flux convergence in the eastern Mohawk valley. The combination of the moisture flux convergence and surface heating where clearing occurred increased the surface equivalent potential temperatures. Additionally, the coldest air aloft arrived at the same time. The tag team of increasing surface equivalent potential temperatures and the arrival of the cold air aloft produced a local maximum in CAPE of greater than $2000\,\mathrm{J\,kg^{-1}}$. Hence, the large hail likely could only happen in the area where it did, facilitated by the overlap of several key features at the right moment: the EML and cold air aloft, the terrain and boundary interactions, and the supercell mesocyclone.

Third, the strengthening ageostrophic circulation across the boundary increased the low-level vertical wind shear. The strong low-level wind shear and its vector alignment with the storm-relative inflow vector implied large values of low-level streamwise vorticity that were comparable with other significant tornadoes (Markowski et al. 2003). The tornado occurred shortly after the supercell crossed the boundary to the cool side, a pattern observed in earlier studies (Markowski et al. 1998). Fourth, the cool side of the boundary had lifting condensation levels that were 400–600 m above ground level, limiting evaporative cooling below cloud level and producing a cold pool with virtual potential temperature perturbations in the hook-echo region that were consistent with other tornadic supercells (Markowski et al. 2002). Similar to the large hail, the tornado likely occurred where mesoscale inhomogeneities came together to maximize the opportunity for a tornado. A caveat is that this is a single case with a high degree of complexity.

Interactions of the terrain with the individual components of the supercell, such as rear- and forward-flank downdrafts, may also have been important for tornadogenesis, but the temporal and spatial observations

available for this case preclude such an analysis. Even with such observations, causality would be challenging. Still, we may hypothesize that the microscale channeling of rear-flank downdraft surges, thermodynamic modification due to upslope or downslope, and terrain-generated vertical vorticity anomalies may all play some role in tornadogenesis in complex terrain.

This one event highlights the potential importance mesoscale inhomogeneities have in locally enhancing the risk for severe weather, especially in areas of complex terrain and when synoptic conditions are ambiguous. This case also highlights the need to continue to improve convection-allowing models, particularly model elements that control the boundary layer moisture, and the advantage mesonet observations may have in resolving important boundaries and mesoscale inhomogeneities. How these mesoscale inhomogeneities interact with convection requires more research, and identifying where these interactions may increase the risk for severe weather is an important forecast problem.

REFERENCES

Atkins, N. T., M. L. Weisman, and L. J. Wicker, 1999: The influence of preexisting boundaries on supercell evolution. *Mon. Wea. Rev.*, **127**, 2910–2927, doi:10.1175/1520-0493(1999)127<2910:TIOPBO>2.0.CO;2.

Banacos, P. C., and M. L. Ekster, 2010: The association of the elevated mixed layer with significant severe weather events in the northeastern United States. *Wea. Forecasting*, **25**, 1082–1102, doi:10.1175/2010WAF2222363.1.

——, ——, J. W. Dellicarpini, and E. J. Lyons, 2012: A multiscale analysis of the 1 June 2011 northeast U.S. severe weather outbreak and associated Springfield, Massachusetts tornado. *Electron. J. Severe Storms Meteor.*, **7** (5). [Available online at http://www.ejssm.org/ojs/index.php/ejssm/article/view/105.]

Bosart, L. F., A. Seimon, K. D. LaPenta, and M. J. Dickinson, 2006: Supercell tornadogenesis over complex terrain: The Great Barrington, Massachusetts, tornado on 29 May 1995. *Wea. Forecasting*, **21**, 897–922, doi:10.1175/WAF957.1.

Braun, S. A., and J. P. Monteverdi, 1991: An analysis of a mesocyclone-induced tornado occurrence in northern California.

Wea. Forecasting, **6**, 13–31, doi:10.1175/1520-0434(1991)006<0013:AAOAMT>2.0.CO;2.

Bunkers, M., D. Barber, R. Thompson, R. Edwards, and J. Garner, 2014: Choosing a universal mean wind for supercell motion prediction. *J. Oper. Meteor.*, **2**, 115–129, doi:10.15191/nwajom.2014.0211.

Carbin, G., 2015: Storm Prediction Center warning coordination meteorologist page. NOAA/Storm Prediction Center. [Available online at http://www.spc.noaa.gov/wcm/.]

Chadwick, R., 2015: Citizen Weather Observer Program. [Available online at http://www.wxqa.com.]

Chronis, T., L. D. Carey, C. J. Schultz, E. V. Schultz, K. M. Calhoun, and S. J. Goodman, 2015: Exploring lightning jump characteristics. *Wea. Forecasting*, **30**, 23–37, doi:10.1175/WAF-D-14-00064.1.

Colle, B. A., K. A. Lombardo, J. S. Tongue, W. Goodman, and N. Vaz, 2012: Tornadoes in the New York metropolitan region: Climatology and multiscale analysis of two events. *Wea. Forecasting*, **27**, 1326–1348, doi:10.1175/WAF-D-12-00006.1.

Conway, J. W., and D. S. Zrnić, 1993: A study of embryo production and hail growth using dual-Doppler and multiparameter radars. *Mon. Wea. Rev.*, **121**, 2511–2528, doi:10.1175/1520-0493(1993)121<2511:ASOEPA>2.0.CO;2.

Cummins, K., and M. Murphy, 2009: An overview of lightning locating systems: History, techniques, and data uses, with an in-depth look at the U.S. NLDN. *IEEE Trans. Electromagn. Compat.*, **51**, 499–518, doi:10.1109/TEMC.2009.2023450.

Davies-Jones, R., 1984: Streamwise vorticity: The origin of updraft rotation in supercell storms. *J. Atmos. Sci.*, **41**, 2991–3006, doi:10.1175/1520-0469(1984)041<2991:SVTOOU>2.0.CO;2.

De Pondeca, M. S. F. V., and Coauthors, 2011: The Real-Time Mesoscale Analysis at NOAAs National Centers for Environmental Prediction: Current status and development. *Wea. Forecasting*, **26**, 593–612, doi:10.1175/WAF-D-10-05037.1.

Draxler, R. R., and G. D. Rolph, 2015: HYSPLIT—Hybrid Single-Particle Lagrangian Integrated Trajectory model. NOAA/Air Resources Laboratory, [Available online at http://www.arl.noaa.gov/HYSPLIT.php.]

Emersic, C., P. L. Heinselman, D. R. MacGorman, and E. C. Bruning, 2011: Lightning activity in a hail-producing storm observed with phased-array radar. *Mon. Wea. Rev.*, **139**, 1809–1825, doi:10.1175/2010MWR3574.1.

Farrell, R. J., and T. N. Carlson, 1989: Evidence for the role of the lid and underrunning in an outbreak of tornadic thunderstorms. *Mon. Wea. Rev.*, **117**, 857–871, doi:10.1175/1520-0493(1989)117<0857:EFTROT>2.0.CO;2.

Geerts, B., T. Andretta, S. Luberda, J. Vogt, Y. Wang, L. Oolman, J. Finch, and D. Bikos, 2009: A case study of a long-lived tornadic mesocyclone in a low-CAPE complex-terrain environment. *Electron. J. Severe Storms Meteor.*, **4** (3). [Available online at http://www.ejssm.org/ojs/index.php/ejssm/article/viewArticle/59.]

Hart, J., C. Mead, P. Bothwell, and R. Thompson, 2015: Storm Prediction Center mesoscale analysis pages. NOAA/Storm Prediction Center. [Available online at http://www.spc.noaa.gov/exper/mesoanalysis/.]

Houston, A. L., and R. B. Wilhelmson, 2007: Observational analysis of the 27 May 1997 central Texas tornadic event. Part I: Prestorm environment and storm maintenance/propagation. *Mon. Wea. Rev.*, **135**, 701–726, doi:10.1175/MWR3300.1.

——, and ——, 2012: The impact of airmass boundaries on the propagation of deep convection: A modeling-based study in a high-CAPE, low-shear environment. *Mon. Wea. Rev.*, **140**, 167–183, doi:10.1175/MWR-D-10-05033.1.

Hurlbut, M. M., and A. E. Cohen, 2014: Environments of northeast U.S. severe thunderstorm events from 1999 to 2009. *Wea. Forecasting*, **29**, 3–22, doi:10.1175/WAF-D-12-00042.1.

Johns, R. H., and R. A. Dorr Jr., 1996: Some meteorological aspects of strong and violent tornado episodes in New England and eastern New York. *Natl. Wea. Dig.*, **20**, 2–12.

Johnson, A. W., and K. E. Sugden, 2014: Evaluation of sounding-derived thermodynamic and wind-related parameters associated with large hail events. *Electron. J. Severe Storms Meteor.*, **9** (5). [Available online at http://www.ejssm.org/ojs/index.php/ejssm/article/viewArticle/137.]

Kumjian, M. R., and A. V. Ryzhkov, 2008: Polarimetric signatures in supercell thunderstorms. *J. Appl. Meteor. Climatol.*, **47**, 1940–1961, doi:10.1175/2007JAMC1874.1.

Lang, T. J., S. A. Rutledge, J. E. Dye, M. Venticinque, P. Laroche, and E. Defer, 2000: Anomalously low negative cloud-to-ground lightning flash rates in intense convective storms observed during STERAO-A. *Mon. Wea. Rev.*, **128**, 160–173, doi:10.1175/1520-0493(2000)128<0160:ALNCTG>2.0.CO;2.

LaPenta, K. D., L. F. Bosart, T. J. Galarneau, and M. J. Dickinson, 2005: A multiscale examination of the 31 May 1998 Mechanicville, New York, tornado. *Wea. Forecasting*, **20**, 494–516, doi:10.1175/WAF875.1.

Lee, B. D., B. F. Jewett, and R. B. Wilhelmson, 2006: The 19 April 1996 Illinois tornado outbreak. Part II: Cell mergers and associated tornado incidence. *Wea. Forecasting*, **21**, 449–464, doi:10.1175/WAF943.1.

Lee, I., 2015: A proposed radar strategy for the prediction and warning of severe hail using polarimetric radar data. NWS Eastern Region Tech. Attachment 2015-03, Bohemia, NY, 37 pp. [Available online at http://www.erh.noaa.gov/er/hq/ssd/erps/ta/ta2015-03.pdf.]

Lemon, L. R., 1998: The radar three-body scatter spike: An operational large-hail signature. *Wea. Forecasting*, **13**, 327–340, doi:10.1175/1520-0434(1998)013<0327:TRTBSS>2.0.CO;2.

MacGorman, D. R., D. W. Burgess, V. Mazur, W. D. Rust, W. L. Taylor, and B. C. Johnson, 1989: Lightning rates relative to tornadic storm evolution on 22 May 1981. *J. Atmos. Sci.*, **46**, 221–251, doi:10.1175/1520-0469(1989)046<0221:LRRTTS>2.0.CO;2.

Maddox, R. A., L. R. Hoxit, and C. F. Chappell, 1980: A study of tornadic thunderstorm interactions with thermal boundaries. *Mon. Wea. Rev.*, **108**, 322–336, doi:10.1175/1520-0493(1980)108<0322:ASOTTI>2.0.CO;2.

Markowski, P. M., and N. Dotzek, 2011: A numerical study of the effects of orography on supercells. *Atmos. Res.*, **100**, 457–478, doi:10.1016/j.atmosres.2010.12.027.

——, E. N. Rasmussen, and J. M. Straka, 1998: The occurrence of tornadoes in supercells interacting with boundaries during VORTEX-95. *Wea. Forecasting*, **13**, 852–859, doi:10.1175/1520-0434(1998)013<0852:TOOTIS>2.0.CO;2.

——, J. M. Straka, and E. N. Rasmussen, 2002: Direct surface thermodynamic observations within the rear-flank downdrafts of nontornadic and tornadic supercells. *Mon. Wea. Rev.*, **130**, 1692–1721, doi:10.1175/1520-0493(2002)130<1692:DSTOWT>2.0.CO;2.

——, C. Hannon, J. Frame, E. Lancaster, A. Pietrycha, R. Edwards, and R. L. Thompson, 2003: Characteristics of vertical wind profiles near supercells obtained from the Rapid Update Cycle. *Wea. Forecasting*, **18**, 1262–1272, doi:10.1175/1520-0434(2003)018<1262:COVWPN>2.0.CO;2.

Murray, J. C., and B. A. Colle, 2011: The spatial and temporal variability of convective storms over the northeast United

States during the warm season. *Mon. Wea. Rev.*, **139**, 992–1012, doi:10.1175/2010MWR3316.1.

NOAA, 2015: Storm events database. [Available online at https://www.ncdc.noaa.gov/stormevents/.]

Perez, A. H., L. J. Wicker, and R. E. Orville, 1997: Characteristics of cloud-to-ground lightning associated with violent tornadoes. *Wea. Forecasting*, **12**, 428–437, doi:10.1175/1520-0434(1997)012<0428:COCTGL>2.0.CO;2.

Peyraud, L., 2013: Analysis of the 18 July 2005 tornadic supercell over the Lake Geneva region. *Wea. Forecasting*, **28**, 1524–1551, doi:10.1175/WAF-D-13-00022.1.

Rasmussen, E. N., and D. O. Blanchard, 1998: A baseline climatology of sounding-derived supercell and tornado forecast parameters. *Wea. Forecasting*, **13**, 1148–1164, doi:10.1175/1520-0434(1998)013<1148:ABCOSD>2.0.CO;2.

——, S. Richardson, J. M. Straka, P. M. Markowski, and D. O. Blanchard, 2000: The association of significant tornadoes with a baroclinic boundary on 2 June 1995. *Mon. Wea. Rev.*, **128**, 174–191, doi:10.1175/1520-0493(2000)128<0174:TAOSTW>2.0.CO;2.

Riley, G. T., and L. F. Bosart, 1987: The Windsor Locks, Connecticut tornado of 3 October 1979: An analysis of an intermittent severe weather event. *Mon. Wea. Rev.*, **115**, 1655–1677, doi:10.1175/1520-0493(1987)115<1655:TWLCTO>2.0.CO;2.

Rogers, J., P. Marsh, and R. Thompson, 2015: Sounding climatology page. NOAA/Storm Prediction Center. [Available online at http://www.spc.noaa.gov/exper/soundingclimo/.]

Rotunno, R., and J. Klemp, 1985: On the rotation and propagation of simulated supercell thunderstorms. *J. Atmos. Sci.*, **42**, 271–292, doi:10.1175/1520-0469(1985)042<0271:OTRAPO>2.0.CO;2.

Rutledge, S. A., and P. V. Hobbs, 1984: The mesoscale and microscale structure and organization of clouds and precipitation in midlatitude cyclones. XII: A diagnostic modeling study of precipitation development in narrow cold-frontal rainbands. *J. Atmos. Sci.*, **41**, 2949–2972, doi:10.1175/1520-0469(1984)041<2949:TMAMSA>2.0.CO;2.

Ryzhkov, A. V., M. R. Kumjian, S. M. Ganson, and A. P. Khain, 2013a: Polarimetric radar characteristics of melting hail. Part I: Theoretical simulations using spectral microphysical modeling. *J. Appl. Meteor. Climatol.*, **52**, 2849–2870, doi:10.1175/JAMC-D-13-073.1.

——, ——, ——, and P. Zhang, 2013b: Polarimetric radar characteristics of melting hail. Part II: Practical implications. *J. Appl. Meteor. Climatol.*, **52**, 2871–2886, doi:10.1175/JAMC-D-13-074.1.

Saunders, C. P. R., and I. M. Brooks, 1992: The effects of high liquid water content on thunderstorm charging. *J. Geophys. Res.*, **97**, 14 671–14 676, doi:10.1029/92JD01186.

Schultz, C. J., W. A. Petersen, and L. D. Carey, 2009: Preliminary development and evaluation of lightning jump algorithms for the real-time detection of severe weather. *J. Appl. Meteor. Climatol.*, **48**, 2543–2563, doi:10.1175/2009JAMC2237.1.

——, ——, and ——, 2011: Lightning and severe weather: A comparison between total and cloud-to-ground lightning trends. *Wea. Forecasting*, **26**, 744–755, doi:10.1175/WAF-D-10-05026.1.

Seimon, A., 1993: Anomalous cloud-to-ground lightning in an F5-tornado-producing supercell thunderstorm on 28 August 1990. *Bull. Amer. Meteor. Soc.*, **74**, 189–203, doi:10.1175/1520-0477(1993)074<0189:ACTGLI>2.0.CO;2.

Soula, S., Y. Seity, L. Feral, and H. Sauvageot, 2004: Cloud-to-ground lightning activity in hail-bearing storms. *J. Geophys. Res.*, **109**, D02101, doi:10.1029/2003JD003669.

Steiger, S. M., R. E. Orville, and L. D. Carey, 2007: Total lightning signatures of thunderstorm intensity over north Texas. Part I: Supercells. *Mon. Wea. Rev.*, **135**, 3281–3302, doi:10.1175/MWR3472.1.

Thompson, R. L., R. Edwards, J. A. Hart, K. L. Elmore, and P. Markowski, 2003: Close proximity soundings within supercell environments obtained from the Rapid Update Cycle. *Wea. Forecasting*, **18**, 1243–1261, doi:10.1175/1520-0434(2003)018<1243:CPSWSE>2.0.CO;2.

Trier, S. B., and C. A. Davis, 2007: Mesoscale convective vortices observed during BAMEX. Part II: Influences on secondary deep convection. *Mon. Wea. Rev.*, **135**, 2051–2075, doi:10.1175/MWR3399.1.

Wasula, A. C., L. F. Bosart, and K. D. LaPenta, 2002: The influence of terrain on the severe weather distribution across interior eastern New York and western New England. *Wea. Forecasting*, **17**, 1277–1289, doi:10.1175/1520-0434(2002)017<1277:TIOTOT>2.0.CO;2.

Weisman, M. L., and J. B. Klemp, 1982: The dependence of numerically simulated convective storms on vertical wind shear and buoyancy. *Mon. Wea. Rev.*, **110**, 504–520, doi:10.1175/1520-0493(1982)110<0504:TDONSC>2.0.CO;2.

Wurman, J., Y. Richardson, C. Alexander, S. Weygandt, and P. F. Zhang, 2007: Dual-Doppler and single-Doppler analysis of a tornadic storm undergoing mergers and repeated tornadogenesis. *Mon. Wea. Rev.*, **135**, 736–758, doi:10.1175/MWR3276.1.